

# A novel 2D graphene oxide modified $\alpha$ -AgVO<sub>3</sub> nanorods: Design, fabrication, and enhanced visible-light photocatalytic performance

Jian WU<sup>a</sup>, Liangyu LI<sup>b</sup>, Xing-ao LI<sup>a</sup>, Xin MIN<sup>b,\*</sup>, Yan XING<sup>a,\*</sup>

<sup>a</sup>New Energy Technology Engineering Lab of Jiangsu Province, School of Science, Nanjing University of Posts & Telecommunications (NUPT), Nanjing 210023, China  
<sup>b</sup>Beijing Key Laboratory of Materials Utilization of Nonmetallic Minerals and Solid Wastes, National Laboratory of Mineral Materials, School of Materials Science and Technology, China University of Geosciences (Beijing), Beijing 100083, China

Received: May 26, 2021; Revised: August 25, 2021; Accepted: September 6, 2021

© The Author(s) 2021.

**Abstract:** Silver vanadates are promising visible-light-responded photocatalysts with suitable bandgap for solar absorption. However, the easy recombination of photogenerated carriers limits their performance. To overcome this obstacle, a novel 2D graphene oxide (GO) modified  $\alpha$ -AgVO<sub>3</sub> nanorods (GO/ $\alpha$ -AgVO<sub>3</sub>) photocatalyst was designed herein to improve the separation of photocarriers. The GO/ $\alpha$ -AgVO<sub>3</sub> was fabricated through a facile *in-situ* coprecipitation method at room temperature. It was found that the as-prepared 0.5 wt% GO/ $\alpha$ -AgVO<sub>3</sub> exhibited the most excellent performance for rhodamine B (RhB) decomposition, with an apparent reaction rate constant 18 times higher than that of pure  $\alpha$ -AgVO<sub>3</sub> under visible-light irradiation. In light of the first-principles calculations and the hetero junction analysis, the mechanism underpinned the enhanced photocatalytic performance was proposed. The enhanced photocatalytic performance was ascribed to the appropriate bandgap of  $\alpha$ -AgVO<sub>3</sub> nanorods for visible-light response and efficient separation of photocarriers through GO nanosheets. This work demonstrates the feasibility of overcoming the easy recombination of photogenerated carriers and provides a valuable GO/ $\alpha$ -AgVO<sub>3</sub> photocatalyst for pollutant degradation.

**Keywords:**  $\alpha$ -AgVO<sub>3</sub>; graphene oxide modified  $\alpha$ -AgVO<sub>3</sub> nanorods (GO/ $\alpha$ -AgVO<sub>3</sub>); photocatalysis; graphene oxide (GO) nanosheets; *in-situ* coprecipitation processing

## 1 Introduction

The elimination of toxic organic dyes that hazarded to water resources and human health has aroused widespread attentions [1–3]. Photocatalysis has been regarded as a promising approach to surmount these concerns, wherein visible-light-driven photocatalysts

play an important role [4,5]. However, currently, there are two limitations that hinder the performance and applications of photocatalysts. One is that the band gap of photocatalyst is not suitable for visible-light absorption [6,7], and the other is the rapid recombination of photogenerated electrons and holes [8]. To cope with these issues, it is appealing to search for novel photocatalysts with fascinating properties [9,10].

Silver vanadium oxides (SVOs), including AgVO<sub>3</sub> [11], Ag<sub>4</sub>V<sub>2</sub>O<sub>7</sub> [12], Ag<sub>3</sub>VO<sub>4</sub> [13], and Ag<sub>2</sub>V<sub>4</sub>O<sub>11</sub> [14], have been widely exploited in the field of catalysis

\* Corresponding authors.

E-mail: X. Min, minx@cugb.edu.cn;

Y. Xing, xingyan618@njupt.edu.cn

owing to their excellent electrical properties, controllable surface, and easy availability. Among these SVOs, monoclinic structured  $\alpha$ -AgVO<sub>3</sub> is one of the most promising visible-light-responsible photocatalyst because the hybridization of V 3d, O 2p, and Ag 4d orbitals can form highly dispersed valence bands with a narrow bandgap [15]. For its potential high performance, photocatalytic properties of  $\alpha$ -AgVO<sub>3</sub> based materials have been explored extensively [16,17]. However, the activity of pristine  $\alpha$ -AgVO<sub>3</sub> is still unsatisfactory owing to the fast recombination of photogenerated electrons and holes, which will reduce the photoreaction rate and thus limit its further applications.

Heterojunction construction is an efficient way to overcome the above obstacles. By designing proper heterostructure, including matched band structure and well-controlled surface, an additional transmission path for the carriers (electrons and holes) can be established at the interface which is helpful to improve the photocatalytic performance. Considering the high chemical stability, large surface area, and high electron mobility, 2D graphene oxide (GO) is regarded as an ideal candidate to act as an electron transmitter [18,19]. For example, enhanced photocatalytic activity has been found in GO/g-C<sub>3</sub>N<sub>4</sub>/MoS<sub>2</sub> ternary hybrid material, wherein the fast charge transfer pathway through GO plays a key role [20]. Based on these facts, the introduction of GO to build graphene oxide modified  $\alpha$ -AgVO<sub>3</sub> (GO/ $\alpha$ -AgVO<sub>3</sub>) nanorod hybrid materials is expected to significantly improve the photocatalytic performance of  $\alpha$ -AgVO<sub>3</sub>.

With this aim, a series of GO/ $\alpha$ -AgVO<sub>3</sub> photocatalysts were designed in this work and were fabricated by a facial *in-situ* coprecipitation method. The structure and morphology of the as-prepared GO/ $\alpha$ -AgVO<sub>3</sub> were systematically characterized. And the photocatalytic performance of GO/ $\alpha$ -AgVO<sub>3</sub> was evaluated using photo decomposition of rhodamine B (RhB) as a model reaction. The dynamic of degradative reaction was also analyzed. Moreover, in order to disclose the possible mechanism that underpins the enhanced photocatalytic performance, the band structure of  $\alpha$ -AgVO<sub>3</sub> was calculated by first-principles calculations based on density functional theory (DFT).

## 2 Experimental

### 2.1 Preparation of $\alpha$ -AgVO<sub>3</sub> nanorods and GO/ $\alpha$ -AgVO<sub>3</sub> photocatalysts

Ammonium metavanadate (NH<sub>4</sub>VO<sub>3</sub>,  $\geq 99\%$ , analytical

reagent purchased from Aladdin Chemical Co., Ltd.), silver nitrate (AgNO<sub>3</sub>,  $\geq 99\%$ , analytical reagent), RhB (purchased from Sinopharm Chemical Reagent Co., Ltd.), and graphene oxide (type SE2430 obtained from the Sixth Elemental Inc.) were used as starting materials. All the reagents were used without further purification.

Pristine  $\alpha$ -AgVO<sub>3</sub> nanorods were fabricated using a coprecipitation method at room temperature. Typically, 1 mmol NH<sub>4</sub>VO<sub>3</sub> and 1 mmol AgNO<sub>3</sub> were dispersed in 40 mL of deionized water, and stirred for 1 h to dissolve completely. The AgNO<sub>3</sub> solution was added into the NH<sub>4</sub>VO<sub>3</sub> solution dropwise under agitation, and then the mixture was stirred continuously for 3 h at room temperature. Then  $\alpha$ -AgVO<sub>3</sub> nanorods were obtained by centrifugation at 6000 r/min for 10 min. The nanorods were washed with distilled water and ethanol for three times and then dried in an oven at 40 °C overnight.

The GO/ $\alpha$ -AgVO<sub>3</sub> photocatalysts were fabricated by a facial *in-situ* directly coprecipitation method. Firstly, GO nanosheets (20 mg) were added to deionized water (100 mL), and the suspension was sonicated for 4 h at 10 °C. Likewise, 1 mmol NH<sub>4</sub>VO<sub>3</sub> and 1 mmol AgNO<sub>3</sub> were prepared separately. The 2D GO nanosheet dispersion with a certain mass fraction ratio (0.5, 1.0, and 2.0 wt%) was added to NH<sub>4</sub>VO<sub>3</sub> solution and stirred for 30 min to reach saturated adsorption of VO<sub>3</sub><sup>-</sup> on the surface of GO. Then, the AgNO<sub>3</sub> solution was dropped into the mixture slowly, and the mixture was stirred continuously for 3 h at room temperature. The as-prepared GO/ $\alpha$ -AgVO<sub>3</sub> hybrid materials were obtained by centrifugation at 6000 r/min for 10 min. The hybrid materials were washed with distilled water and ethanol three times and then dried in an oven at 40 °C. For brevity, the as-synthesized photocatalysts were referred as 0.5 GO/ $\alpha$ -AgVO<sub>3</sub>, 1.0 GO/ $\alpha$ -AgVO<sub>3</sub>, and 2.0 GO/ $\alpha$ -AgVO<sub>3</sub> according to the GO weight percentage hereafter.

### 2.2 Structural characterization and photocatalytic activity

The phase compositions of the  $\alpha$ -AgVO<sub>3</sub> and GO/ $\alpha$ -AgVO<sub>3</sub> were characterized by X-ray diffraction (XRD) on a Bruker D8 diffractometer with Cu K $\alpha$  radiation ( $\lambda = 1.5418 \text{ \AA}$ ). The morphology characterizations were conducted on a Hitachi S-4800 scanning electron microscope (SEM) equipped with energy dispersive spectroscopy (EDS) for elemental analysis. Transmission electron microscopy (TEM) and high-resolution TEM

were performed on a Hitachi HT7700 with an accelerating voltage of 200 kV. Ultraviolet visible (UV–Vis) diffuse reflectance spectra (DRS) were carried out on a UV–Vis spectrophotometer (UV-3600 PLUS) equipped with an integrating sphere device in the wavelength range of 300–800 nm. Ultraviolet photoelectron spectroscopy (UPS) was characterized with He I (21.22 eV) as the monochromatic light source and the total energy resolution is 100 meV. The X-ray photoelectron spectroscopy (XPS) measurements were carried out on ESCALAB 250Xi with an Al K $\alpha$  source to identify surface chemical composition and chemical states. Zeta potential was measured by Zetapals (Brookhaven, USA). Brunauer–Emmett–Teller (BET) surface area was analyzed on an Autosorb-iQ2-MP (Quantachrome Instruments, USA) and calculated by its embedded ASiQwin software using BET model. All the samples (100 mg) were degassed at 300 °C for 6 h. The N<sub>2</sub> isotherms were recorded at 77 K. Photoluminescence (PL) spectra were recorded on a Shimadzu RF-6000 Plus fluorescence spectrometer with an excitation wavelength of 400 nm.

The photocatalytic activities of the as-prepared  $\alpha$ -AgVO<sub>3</sub> and GO/ $\alpha$ -AgVO<sub>3</sub> were evaluated via the photodegradation efficiency of RhB. The experiments were carried out in a photoreactor containing a 300 W Xenon lamp (400 nm cutoff filter) and a circulating cooling water system. For the catalytic experiments, 15 mg of the as-prepared samples were dispersed in 30 mL RhB solution (5 mg/L) and stirred for 30 min in dark to reach the adsorption–desorption equilibrium. Then, the light source was switched on to start the photoreaction, during which, the residual concentration of RhB was monitored by UV–Vis absorption spectra at certain time intervals. The degradation efficiency was calculated from the absorbance of the dye solution at a wavelength of 552 nm. Since the zeta potentials of GO,  $\alpha$ -AgVO<sub>3</sub>, and GO/ $\alpha$ -AgVO<sub>3</sub> are –26.20, –32.47, and –34.63 mV, respectively, demonstrating that their surfaces are negatively charged, they were well dispersed during the photocatalytic experiments.

### 2.3 Band structure calculation

The band structure of  $\alpha$ -AgVO<sub>3</sub> was investigated to understand its photocatalytic performance. For this aim, first-principles calculations were conducted using the Cambridge serial total energy package (CASTEP) code [21,22]. The plane-wave basis set cutoff was 760 eV after convergent test. A 2×2×3 Monkhorst-Pack

$k$ -mesh was used to sample the Brillouin zone of  $\alpha$ -AgVO<sub>3</sub> [23]. Geometry optimization was conducted via the Perdew–Burke–Ernzerhof (PBE) exchange–correlation function within the generalized gradient approximation (GGA) [24]. The convergence tolerance for the total energy and maximum ionic displacement was set as  $1.0\times 10^{-5}$  eV and  $1.0\times 10^{-3}$  Å, respectively. After completing the geometry optimization, an OTFG ultrasoft potential and GGA functional was used to calculate the band structure of  $\alpha$ -AgVO<sub>3</sub>. To further improve the accuracy of band gap calculation, a hybrid HSE03 exchange–correlation functional was employed which has been proven in obtaining a reliable bandgap for complex oxides [25].

## 3 Results

### 3.1 Morphology of $\alpha$ -AgVO<sub>3</sub> and GO/ $\alpha$ -AgVO<sub>3</sub>

Figure 1 shows the morphologies of the  $\alpha$ -AgVO<sub>3</sub> and GO/ $\alpha$ -AgVO<sub>3</sub> with various weight percentages of GO. As shown in Fig. 1(a), the pure  $\alpha$ -AgVO<sub>3</sub> sample shows a flower-like morphology, which is composed of plentiful one-dimensional (1D)  $\alpha$ -AgVO<sub>3</sub> nanorods with a length of 10–15  $\mu$ m and a width of 100–300 nm. Figures 1(b)–1(d) show the morphologies of 0.5 GO/ $\alpha$ -AgVO<sub>3</sub>, 1.0 GO/ $\alpha$ -AgVO<sub>3</sub>, and 2.0 GO/ $\alpha$ -AgVO<sub>3</sub>, respectively. The  $\alpha$ -AgVO<sub>3</sub> nanorods are covered by 2D GO nanosheets, indicating the formation of heterojunctions. Notably, with the increase of GO content, the accumulation of a large amount of lamellar corrugated GO nanosheets can be observed. Meanwhile, the introduction of GO also increases the BET surface area of the GO/ $\alpha$ -AgVO<sub>3</sub> nanocomposites (Fig. S1 and Table S1 in the Electronic Supplementary Material (ESM)). TEM and high-resolution TEM (HRTEM) were used to further characterize the microstructure of GO/ $\alpha$ -AgVO<sub>3</sub> composites. As shown in Fig. 1(e),  $\alpha$ -AgVO<sub>3</sub> exhibits a nanorod structure with corrugated GO nanosheets tightly attached on it. The HRTEM image in Fig. 1(f) shows that the lattice fringes of 0.27 nm can be indexed to the (002) lattice planes of  $\alpha$ -AgVO<sub>3</sub>. The inset image of Fig. 1(f) is the corresponding SAED pattern. The composition of GO/ $\alpha$ -AgVO<sub>3</sub> photocatalyst was further characterized by EDS elemental mapping. As shown in Fig. 2, silver, oxygen, and vanadium elements are uniformly distributed on the nanorods, and the corrugated nanosheets correspond to the carbon element, indicating the close coupling of  $\alpha$ -AgVO<sub>3</sub> nanorods and GO nanosheets.

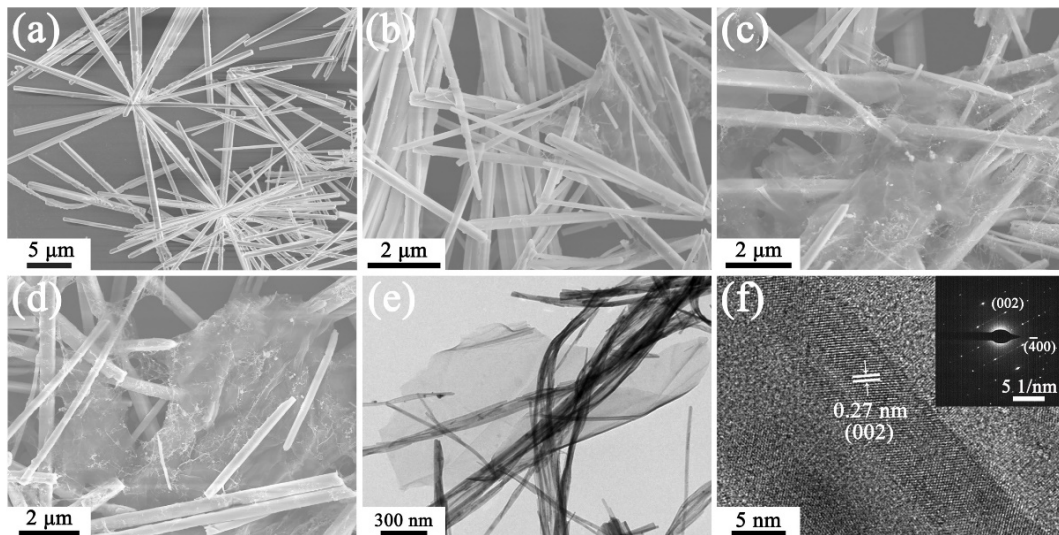


**Fig. 1** SEM images of the as-prepared (a)  $\alpha$ -AgVO<sub>3</sub>, (b) 0.5 GO/ $\alpha$ -AgVO<sub>3</sub>, (c) 1.0 GO/ $\alpha$ -AgVO<sub>3</sub>, and (d) 2.0 GO/ $\alpha$ -AgVO<sub>3</sub>, and (e) TEM image and (f) HRTEM image of 0.5 GO/ $\alpha$ -AgVO<sub>3</sub> (the inset image in (f) shows the corresponding SAED pattern).

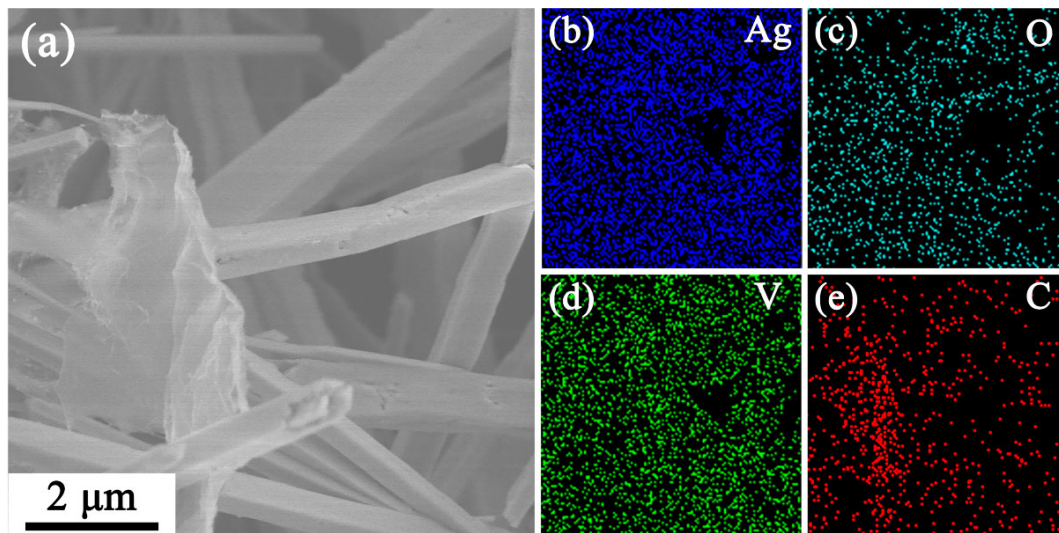


**Fig. 2** SEM image of (a) 0.5 GO/ $\alpha$ -AgVO<sub>3</sub> and the corresponding EDS elemental mappings of (b) Ag, (c) O, (d) V, and (e) C.

### 3. 2 Crystal structure and XRD analysis

The phase composition and preferred growth direction of  $\alpha$ -AgVO<sub>3</sub> nanorods were further studied by experimental and simulated XRD patterns. The XRD patterns of the as-prepared  $\alpha$ -AgVO<sub>3</sub> and GO/ $\alpha$ -AgVO<sub>3</sub> are shown in Fig. 3. The  $\alpha$ -AgVO<sub>3</sub> is well crystallized in a monoclinic structure and no impurity phase can be detected. The main peaks at  $2\theta$  of 12.40°, 17.22°, 24.95°, 27.50°, 28.23°, 31.51°, 32.12°, and 32.82°, can be ascribed to (110), (200), (220), (310), ( $\bar{2}$ 21), (221), ( $\bar{1}$ 31), and (002) diffraction planes of  $\alpha$ -AgVO<sub>3</sub> (according to JCPDS Card #89-4396), respectively. After the introduction of GO, the  $2\theta$  angles of these diffraction peaks remain unchanged, indicating that the

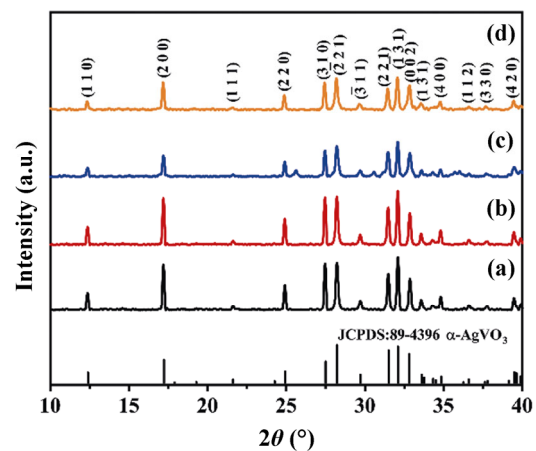


**Fig. 3** XRD patterns of (a)  $\alpha$ -AgVO<sub>3</sub>, (b) 0.5 GO/ $\alpha$ -AgVO<sub>3</sub>, (c) 1.0 GO/ $\alpha$ -AgVO<sub>3</sub>, and (d) 2.0 GO/ $\alpha$ -AgVO<sub>3</sub>.

addition of GO does not affect the phase stability and crystal structure of  $\alpha$ -AgVO<sub>3</sub>. Due to the low percentage and weak reflection of GO, no obvious diffraction peak for GO can be observed in the XRD pattern of GO/ $\alpha$ -AgVO<sub>3</sub>.

To reveal the growth direction of  $\alpha$ -AgVO<sub>3</sub> nanorods, its crystal structure was constructed and optimized (Fig. 4 and Table 1), and the comparison of the simulated and experimental XRD patterns of  $\alpha$ -AgVO<sub>3</sub> is shown in Fig. 5. As shown in Fig. 4, two VO<sub>4</sub> tetrahedrons are connected by sharing vertex and then precipitate with Ag to crystallize in a monoclinic  $\alpha$  phase AgVO<sub>3</sub> with space group *C2/c*. The geometry optimized lattice constants, atomic positions, and bond lengths of  $\alpha$ -AgVO<sub>3</sub> are shown in Table 1.

Based on this geometry optimized crystal structure, the XRD pattern simulation was carried out through the Reflex code in Materials Studio software (Accelrys Software Inc., San Diego, CA, USA) using Cu K $\alpha$  radiation of  $\lambda = 1.5406 \text{ \AA}$ , and step size of  $0.02^\circ$ . The preferred *c*-axis orientation was imposed by the Rietveld–Toraya method and the simulated morphology

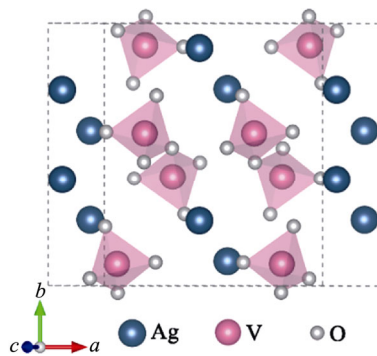


Fig. 4 Crystal structure of  $\alpha$ -AgVO<sub>3</sub>.

was generated based on the theory of Donnay and Harker [26], Wells [27], and Berkovitch-Yellin [28]. According to Scherrer's formula, the grain size difference in different directions will result in different degrees of broadening of diffraction peaks. Thus, as shown in Fig. 5, the simulated XRD pattern of  $\alpha$ -AgVO<sub>3</sub> nanorods with a growth direction that perpendicular to the (002) crystal plane is closer to the experimental result, compared with that of the power reflection without orientation. Meanwhile, the simulated morphology shown in Fig. 5(d) further confirms that the  $\alpha$ -AgVO<sub>3</sub> nanorods prefer to grow along *c*-axis that is perpendicular to

**Table 1** Geometry optimized lattice constants, atomic positions, and bond lengths of  $\alpha$ -AgVO<sub>3</sub>

Parameter	$\alpha$ -AgVO <sub>3</sub>		
Space group	<i>C2/c</i> (No. 15)		
Lattice constant	$a = 11.2975 \text{ \AA}$		
	$b = 10.7962 \text{ \AA}$		
	$c = 5.78487 \text{ \AA}$		
	$V = 646.534 \text{ \AA}^3$		
Atomic position	V1 (0.30349, 0.41734, 0.26496)		
	Ag1 (0, 0.25195, 0.25)		
	Ag2 (0, 0.59393, 0.25)		
	O1 (0.13789, 0.41143, 0.14139)		
	O2 (0.14649, 0.027, -0.02306)		
	O3 (0.36723, 0.27405, 0.36506)		
Bond length	Bond	Population	Bond length ( $\text{\AA}$ )
	O–V	0.73	1.70684
	O–V	0.73	1.71587
	O–Ag	0.22	2.17526
	O–Ag	0.24	2.14763
	O–O	0.00	2.81117

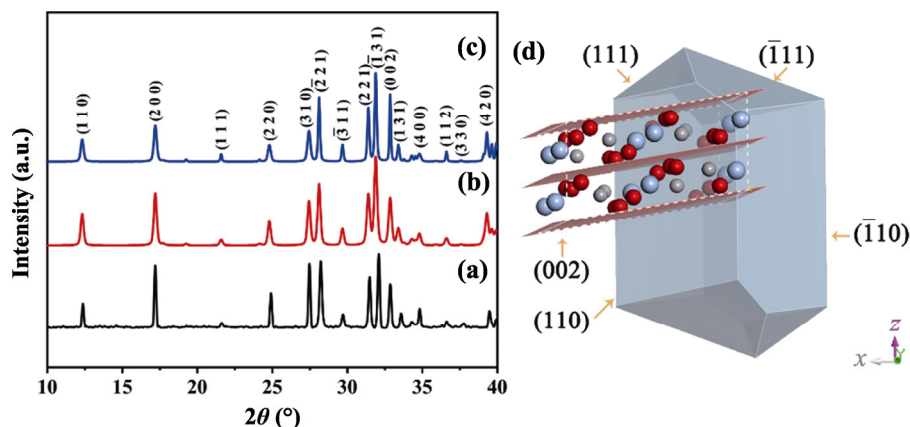


Fig. 5 (a) Experimental XRD patterns of  $\alpha$ -AgVO<sub>3</sub>, together with simulated XRD patterns of (b) powder and (c) *c*-axis oriented particle, and (d) morphology of  $\alpha$ -AgVO<sub>3</sub> generated based on the theory of Donnay–Harker (in the crystal structure of  $\alpha$ -AgVO<sub>3</sub>, (002) plane is highlighted).

(002) crystal plane, which is in accordance with the TEM results.

### 3.3 FTIR and Raman characterization

In order to confirm the presence of GO in the GO/ $\alpha$ -AgVO<sub>3</sub> photocatalysts, Fourier transform infrared spectroscopy (FTIR spectroscopy) and Raman spectroscopy were employed. As shown in the FTIR spectra (Fig. 6(a)), the bands related to the VO<sub>4</sub> tetrahedron, including  $\nu$  (V–O–V, 515 cm<sup>-1</sup>),  $\delta$  (V–O, 636 cm<sup>-1</sup>), and  $\nu$  (V = O, 660, 895, 929, and 964 cm<sup>-1</sup>) vibrational modes are observed, as well as bands at 846 cm<sup>-1</sup> for  $\nu$  (Ag–O–V) stretching modes [29,30]. For GO/ $\alpha$ -AgVO<sub>3</sub>, in addition to the bands mentioned above, typical peaks of C–O stretching and C–C sp<sup>2</sup> in-plane vibration emerge at 1057 and 1624 cm<sup>-1</sup>, demonstrating the successfully introduction of GO [31]. In fact, GO is more sensitive to Raman spectroscopy. As shown in Fig. 6(b), two typical GO peaks at about 1340 and 1597 cm<sup>-1</sup> appear in the spectra of GO/ $\alpha$ -AgVO<sub>3</sub>, which are attributed to the disordered sp<sup>2</sup> carbon (D-band) and well-ordered graphite (G-band), respectively [32,33]. With the increase of GO contents, the intensity of D and G peaks also increases. Moreover, the main characteristic vibration peaks of  $\alpha$ -AgVO<sub>3</sub> are all observed. In Raman spectra of all the samples, the strongest band at 919 cm<sup>-1</sup> may originate from symmetric stretching of V–O–Ag or O–V–O vibrations. The band at 897 cm<sup>-1</sup> is linked with the stretching vibrations of Ag–O–Ag, while the band at 875 cm<sup>-1</sup> represents the stretching vibrations of the V–O–Ag. The bands appearing at 850, 762, 627, and 528 cm<sup>-1</sup> are related to the asymmetric and symmetric stretching modes of V–O–V [34–36]. Based on the FTIR and Raman spectrum analysis, the presence

of GO in GO/ $\alpha$ -AgVO<sub>3</sub> nanocomposites is further confirmed. All the foregoing results demonstrate that a series of  $\alpha$ -AgVO<sub>3</sub> (002)//GO (002) heterostructure photocatalysts have been successfully prepared.

### 3.4 Photocatalytic performance

The photocatalytic activities of  $\alpha$ -AgVO<sub>3</sub> and GO/ $\alpha$ -AgVO<sub>3</sub> are evaluated in terms of the photo degradation of RhB. Figure 7(a) shows the variation of RhB concentration versus irradiation time of visible light. It is obvious that the introduction of GO significantly improves the photocatalytic performance compared with pure  $\alpha$ -AgVO<sub>3</sub>. After 40 min of irradiation, the 0.5 GO/ $\alpha$ -AgVO<sub>3</sub> photocatalyst displays the highest photocatalytic activity with 90.0% RhB degradation, while less RhB is removed by pure  $\alpha$ -AgVO<sub>3</sub>. Quantitatively, the photocatalytic degradation of RhB can be described by pseudo-first-order dynamic process and its kinetics can be expressed as

$$\ln\left(\frac{C_0}{C}\right) = k_1 t \quad (1)$$

where  $C$  is the concentration of the RhB at time  $t$ ,  $C_0$  is the initial concentration of the RhB solution, and the slope  $k_1$  is the apparent reaction rate constant. As shown in Fig. 7(b), the 0.5 GO/ $\alpha$ -AgVO<sub>3</sub> photocatalyst has the maximum rate constant of 0.0584 min<sup>-1</sup> which is 18 times higher than that of pure  $\alpha$ -AgVO<sub>3</sub>, revealing the superior photocatalytic activity of the GO/ $\alpha$ -AgVO<sub>3</sub>. With the increase of GO contents, the degradation efficiency decreases probably due to the aggregation of GO nanosheets as shown in SEM images in Fig. 1. Moreover, the photocatalytic activity of the GO/ $\alpha$ -AgVO<sub>3</sub> shows good stability. As shown in Fig. 7(c), after three

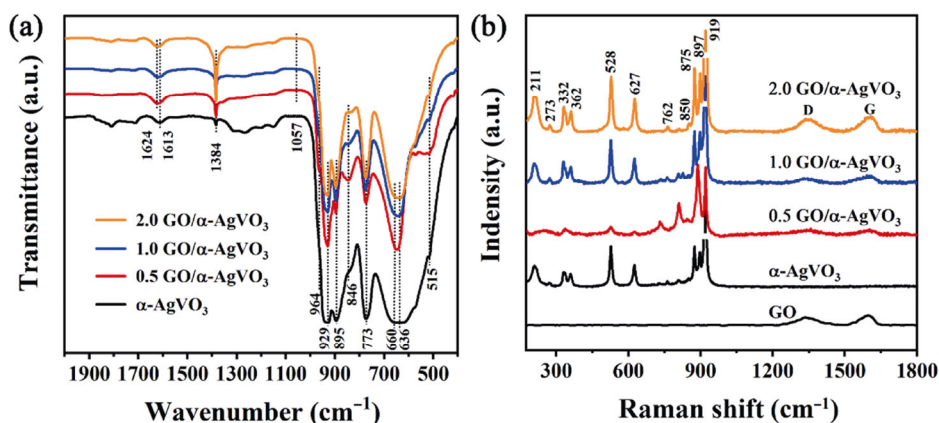


**Fig. 6** (a) FTIR spectra and (b) Raman spectra of  $\alpha$ -AgVO<sub>3</sub> and GO/ $\alpha$ -AgVO<sub>3</sub> nanocomposites with different GO contents (0.5, 1.0, and 2.0 wt%).

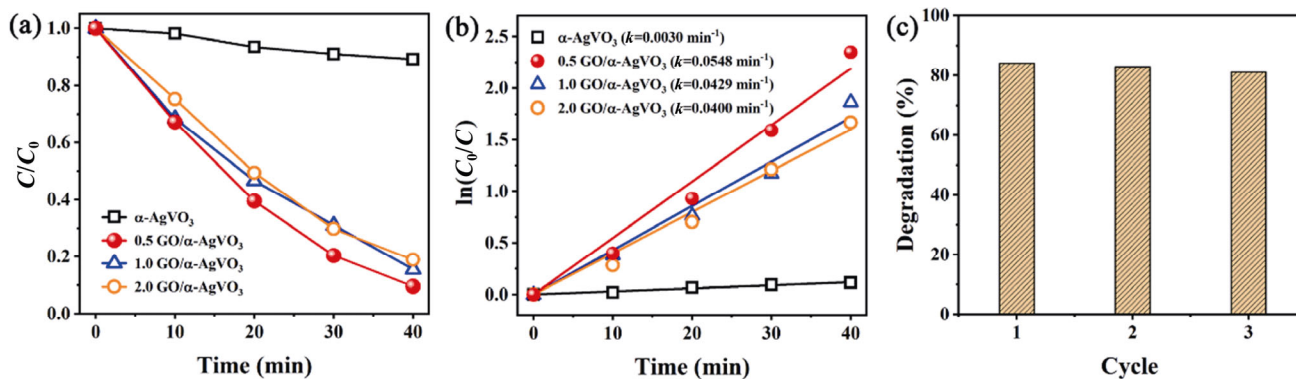


**Fig. 7** (a) Photocatalytic degradation curves of RhB, (b) corresponding pseudo-first-order kinetic curves, and (c) cyclic tests of the 0.5 GO/ $\alpha$ -AgVO<sub>3</sub>.

**Table 2** RhB photodegradation properties of recently reported SVOs and other photocatalysts

Photocatalyst	Loading photocatalyst (mg)/dye (mg)	Light source	Degradation ratio <sup>a</sup>	Apparent rate constant, $k$ ( $\text{min}^{-1}$ )	Reference
TiO <sub>2</sub>	100/1	Xe, 300 W, > 400 nm	12%	0.0060	Wang <i>et al.</i> [37]
$\alpha$ -AgVO <sub>3</sub> / $\alpha$ -FeOOH	50/0.24	Xe, 500 W, > 420 nm	45%	0.0194	Sun <i>et al.</i> [17]
$\beta$ -AgVO <sub>3</sub> /Ag <sub>3</sub> VO <sub>4</sub>	50/0.3	Xe, 300 W, > 400 nm	76%	0.0340	Gao <i>et al.</i> [38]
$\beta$ -AgVO <sub>3</sub> /BiVO <sub>4</sub>	50/1	Xe, 300 W, > 400 nm	69%	0.0206	Wang and Cao [39]
$\beta$ -AgVO <sub>3</sub> /AgBr	30/0.5	Xe, 800 W, 420–780 nm	23%	0.0183	Zhang <i>et al.</i> [40]
Ag <sub>4</sub> V <sub>2</sub> O <sub>7</sub>	80/0.38	Xe, 500 W, 420–800 nm	38%	—	Wang <i>et al.</i> [41]
g-C <sub>3</sub> N <sub>4</sub> /Ag <sub>4</sub> V <sub>2</sub> O <sub>7</sub>	100/1	Xe, 300 W, > 420 nm	55%	0.015	Zhang <i>et al.</i> [42]
Ag <sub>3</sub> VO <sub>4</sub>	2000/4.8	Xe, 500 W, > 420 nm	32%	0.0155	Zhang <i>et al.</i> [43]
GO/ $\alpha$ -AgVO <sub>3</sub>	15/0.15	Xe, 300 W, > 420 nm	90%	0.0584	This work

<sup>a</sup>The degradation percentage is collected at 40 min visible-light irradiation for better comparison.

continuous cyclic tests, RhB can still be degraded under visible-light irradiation. The above results demonstrate that compared with other SVOs and traditional TiO<sub>2</sub> photocatalysts under the similar experimental conditions [17,37–43], the GO/ $\alpha$ -AgVO<sub>3</sub> photocatalyst shows outstanding performance with fast rate and large degradation ratio as shown in Table 2.

## 4 Discussion

### 4.1 Electronic structure and bandgaps

To shed light on the photocatalytic mechanism, it is necessary to analyze the electronic structure of  $\alpha$ -AgVO<sub>3</sub>. Figure 8 shows the band structure of  $\alpha$ -AgVO<sub>3</sub> along the high symmetry line in the Brillouin zone calculated by GGA (Fig. 8(a)) and HSE03 functional (Fig. 8(b)). The  $\alpha$ -AgVO<sub>3</sub> is a direct band gap semiconductor because the top of valence bands and bottom of conduction bands are at the Gamma point simultaneously. The direct band gap of  $\alpha$ -AgVO<sub>3</sub> obtained from GGA

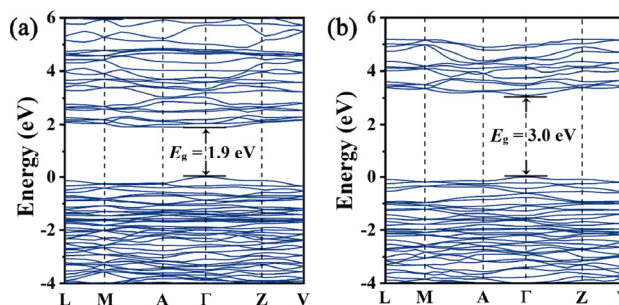


**Fig. 8** Band structure of  $\alpha$ -AgVO<sub>3</sub> along the high symmetry line in the Brillouin zone calculated by (a) GGA and (b) HSE03 functional.

functional is 1.9 eV because the GGA functional generally underestimates the experimental bandgaps. To improve the accuracy of bandgap calculation, a hybrid functional [44] based on a screened Coulomb potential HSE03 was used in DFT calculation. As shown in Fig. 8(b), the band gap obtained by HSE03 functional is 3.0 eV, which is believed more reliable and closer to the experimental values for complex oxides [25,45].

To analyze the optical properties and obtain the

experimental bandgaps, UV–Vis absorption spectra of  $\alpha$ -AgVO<sub>3</sub> and GO/ $\alpha$ -AgVO<sub>3</sub> nanorods are collected. As shown in Fig. 9(a), the absorbance edge of  $\alpha$ -AgVO<sub>3</sub> is around 540 nm. After the introduction of 0.5 and 1.0 wt% GO, the absorption band edge shows an obvious blue-shift, while 2.0 wt% GO addition causes the absorption band edge to shift in the opposite direction. The change of absorption edge is closely related to the band gap, which can be obtained by the Kubelka–Munk method [46].

$$(\alpha h\nu)^n = A(h\nu - E_g) \quad (2)$$

where  $\alpha$ ,  $h$ ,  $\nu$ ,  $A$ , and  $E_g$  are the absorption coefficient, Planck’s constant, light frequency, proportionality constant, and optical bandgap, respectively. The index  $n$  depends on the electronic transition of the crystalline semiconductor,  $n = 0.5$  for indirect-gap semiconductor and  $n = 2$  for direct-gap semiconductor. For  $\alpha$ -AgVO<sub>3</sub> crystal,  $n$  equals 2, because  $\alpha$ -AgVO<sub>3</sub> is a direct transition type of semiconductors, according to the band structure in Fig. 8. The Kubelka–Munk plots are shown in Fig. 9(b). The band gap energy can be estimated from the

intercept of the tangent to the plot of  $(\alpha h\nu)^2$  vs. energy ( $h\nu$ ). The band gap of  $\alpha$ -AgVO<sub>3</sub> is 2.56 eV, which is approximate to the calculated bandgap from HSE03. The bandgaps for 0.5, 1.0, and 2.0 GO/ $\alpha$ -AgVO<sub>3</sub> are 2.59, 2.62, and 2.26 eV, respectively, i.e., the addition of 0.5 and 1.0 wt% GO can help to increase the band gap, which is beneficial for the separation of photogenerated carriers. However, continuing to increase the GO content will narrow the bandgap due to the conductive nature of GO, resulting in the decrease of photocatalytic performance. Therefore, the theoretical and experimental analysis of band structure demonstrates that  $\alpha$ -AgVO<sub>3</sub> is a visible-light-responsible photocatalyst, and the combination with an appropriate amount of GO helps to adjust the band gap and improve the photocatalytic efficiency.

To further analyze the band structure, UPS is implemented to ascertain the valence band energy ( $E_v$ ), as shown in Fig. 10(a). The  $E_v$  of  $\alpha$ -AgVO<sub>3</sub> is calculated to be 6.61 eV via subtracting the width of the UPS spectra from the excitation energy of 21.22 eV [47]. The conduction band energy ( $E_c$ ) is thus estimated at

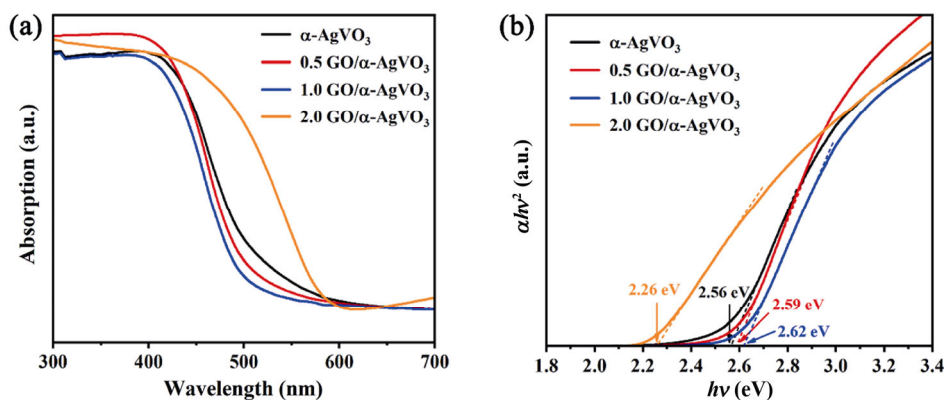


Fig. 9 (a) UV–Vis diffuse reflectance spectra and (b) Kubelka–Munk plots of  $\alpha$ -AgVO<sub>3</sub> and GO/ $\alpha$ -AgVO<sub>3</sub> nanocomposites with different GO contents (0.5, 1.0, and 2.0 wt%).

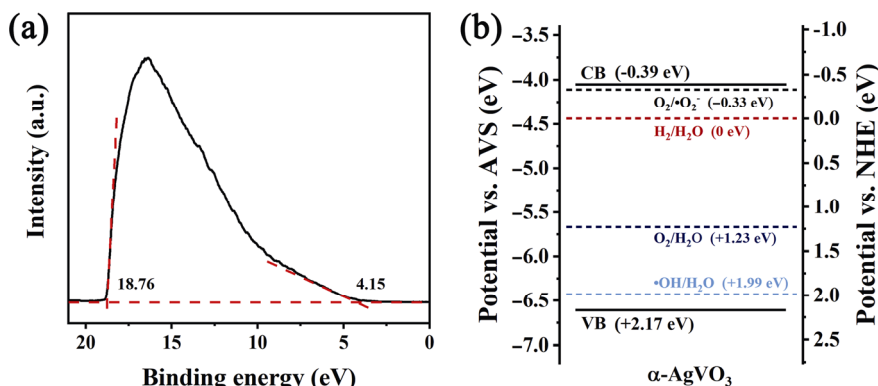


Fig. 10 (a) UPS spectra and (b) band structure diagram of  $\alpha$ -AgVO<sub>3</sub>.

4.05 eV from the equation:  $E_c = E_v - E_g$ . Considering the reference standard for which 0 eV vs. normal hydrogen electrode (NHE) equals  $-4.44$  eV vs.  $E_{avs}$  (vacuum level), the  $E_v$  and  $E_c$  of  $\alpha$ -AgVO<sub>3</sub> are converted to  $-0.39$  and  $2.17$  eV (vs. NHE), respectively [48]. The energy position of  $\alpha$ -AgVO<sub>3</sub> is illustrated in Fig. 10(b) [49], which provides clear guidance for the subsequent proposal of the photocatalytic mechanism.

## 4.2 Role of GO/ $\alpha$ -AgVO<sub>3</sub> heterojunction

According to the structure and morphology characterization and simulated morphology in Section 3, the  $\alpha$ -AgVO<sub>3</sub> (002)//GO (002) heterojunction is successfully constructed in the GO/ $\alpha$ -AgVO<sub>3</sub> photocatalyst. The surface chemical composition and the interaction of GO and  $\alpha$ -AgVO<sub>3</sub> were further confirmed by XPS. The full range XPS spectrum in Fig. 11(a) confirms the presence of C, Ag, V, and O elements in the 0.5 GO/ $\alpha$ -AgVO<sub>3</sub> without impurities. The atomic ratio of Ag, V, and O is 12.1%:22.0%:65.9%, which is close to the stoichiometric ratio of  $\alpha$ -AgVO<sub>3</sub>. The high-resolution XPS spectra of Ag 3d, V 2p, and O 1s are shown in Figs. 11(b)–11(d), respectively. In Fig. 11(b), the peaks that emerged at the binding energies of 367.5 and 373.5 eV correspond to Ag 3d<sub>5/2</sub> and Ag 3d<sub>3/2</sub> orbits,

respectively. The XPS spectra of V 2p show two specific peaks of pentavalent vanadium at the binding energies of 516.4 and 523.8 eV [50], as shown in Fig. 11(c). The O 1s spectrum shown in Fig. 11(d) can be split into three peaks at 529.9, 530.4, and 532.1 eV, which are attributed to the binding energies of lattice oxygen, oxygen defects, and adsorbed oxygen species, respectively [51]. After the introduction of GO, a new C = O peak appears at 533.4 eV in the O 1s spectrum [52]. More importantly, peaks of Ag 3d, V 2p, and O 1s in 0.5, 1.0, and 2.0 GO/ $\alpha$ -AgVO<sub>3</sub>, respectively, all shift towards the high binding energy, indicating that the electron migration from  $\alpha$ -AgVO<sub>3</sub> to GO nanosheet happens, which can improve the separation efficiency of photogenerated carriers and enhance photocatalytic performance [13]. The photoluminescence spectra with excited wavelength of 400 nm are shown in Fig. 12. In comparison with pure  $\alpha$ -AgVO<sub>3</sub> nanorods, the PL emission intensities of 0.5 and 1.0 GO/ $\alpha$ -AgVO<sub>3</sub> nanocomposites are significantly weaker, demonstrating that the 0.5 and 1.0 GO/ $\alpha$ -AgVO<sub>3</sub> nanocomposites own better separation ability for photogenerated charges, which will enhance the photocatalytic activity. The 2.0 GO/ $\alpha$ -AgVO<sub>3</sub> nanocomposite with higher GO content shows a relatively higher PL emission intensity and

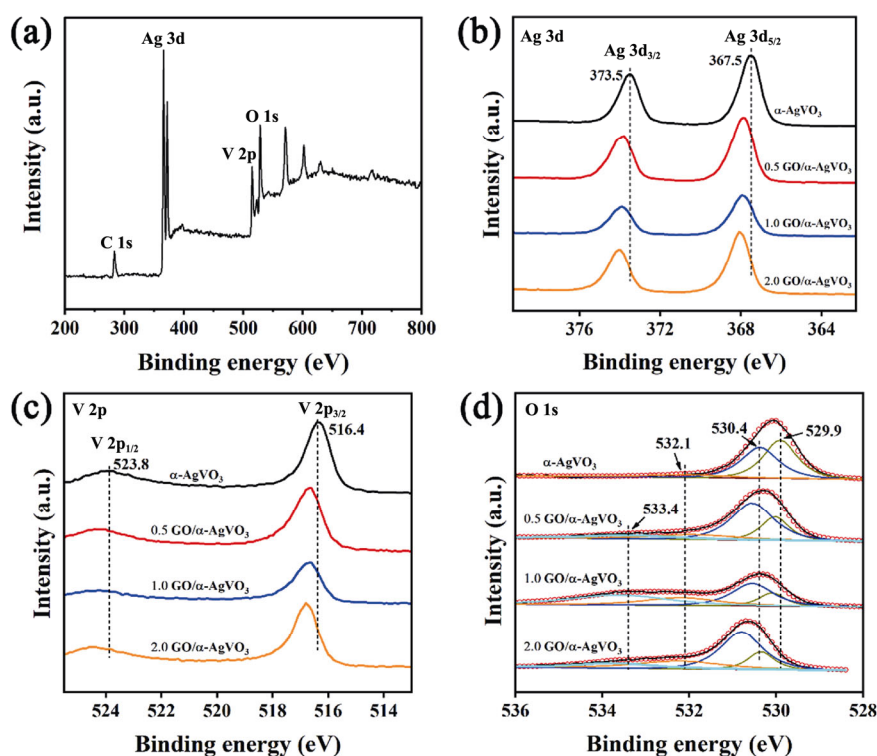


**Fig. 11** (a) Full-scale XPS survey spectrum for 0.5 GO/ $\alpha$ -AgVO<sub>3</sub> and the XPS spectra of (b) Ag 3d, (c) V 2p, and (d) O 1s for GO/ $\alpha$ -AgVO<sub>3</sub> with different GO contents (0.5, 1.0, and 2.0 wt%).

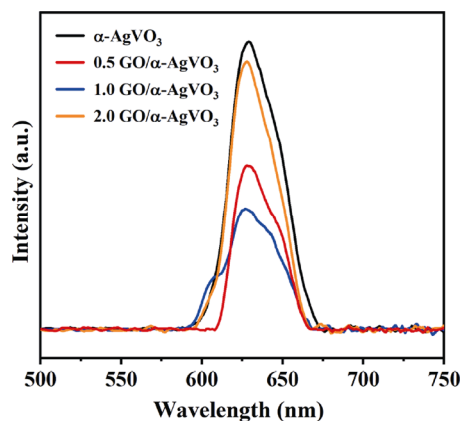


**Fig. 12** PL spectra of pure  $\alpha$ -AgVO<sub>3</sub> nanorods and GO/ $\alpha$ -AgVO<sub>3</sub> nanocomposites with different amount of GO.

lower photocatalytic efficiency, which may be due to the fast recombination of photo-induced electron–hole pairs on the aggregated GO without forming the heterostructure.

### 4.3 Mechanism for the enhanced photocatalytic performance of the GO/ $\alpha$ -AgVO<sub>3</sub>

Based on the foregoing analysis, the possible mechanism of the GO/ $\alpha$ -AgVO<sub>3</sub> photocatalyst is proposed and illustrated in Fig. 13. When the visible-light shines on the surface of GO/ $\alpha$ -AgVO<sub>3</sub> photocatalyst, the electrons ( $e^-$ ) at valance band (VB) are excited to conduct band (CB), leaving an equal number of holes ( $h^+$ ) at VB, as presented in Eq. (3) [53]. The electrons in the conduction band of  $\alpha$ -AgVO<sub>3</sub> can be transferred to the surface of GO through the  $\alpha$ -AgVO<sub>3</sub> (002)//GO (002) heterojunction, promoting the separation efficiency of photogenerated carriers. Taking advantage of the conductivity of GO's  $\pi$ - $\pi$  graphitic carbon network, the lifetime of electrons can be further prolonged [54], which is helpful to improve the photocatalytic performance. Then, the  $h^+$  at VB can produce hydroxyl radicals ( $\bullet$ OH) by reacting with H<sub>2</sub>O, while the  $e^-$  at GO can generate superoxide radicals [13]. These radicals and holes with high oxidative activity can degrade organic pollutants like RhB efficiently by the following possible equations:

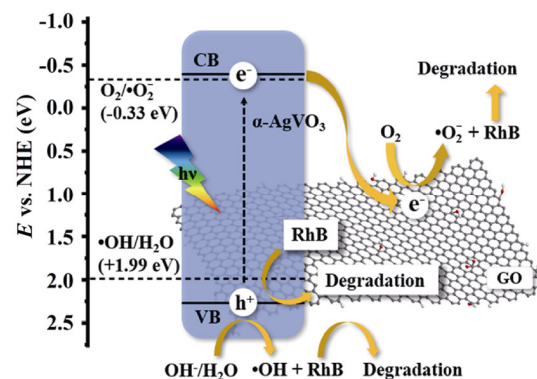
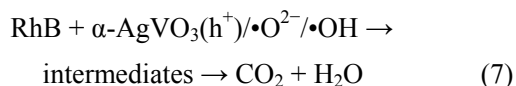
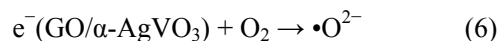
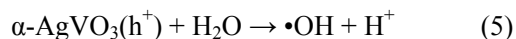


**Fig. 13** Proposed photocatalytic mechanism of GO/ $\alpha$ -AgVO<sub>3</sub> photocatalyst.

Therefore, suitable band structure and bandgap for visible-light absorption are fundamental factors for visible-light-responsive photocatalyst, and their photocatalytic performance can be further improved by inhibiting the recombination of photogenerated carriers through heterostructure design.

## 5 Conclusions

In summary, novel visible-light-responded photocatalysts including 0.5 wt% GO/ $\alpha$ -AgVO<sub>3</sub>, 1.0 wt% GO/ $\alpha$ -AgVO<sub>3</sub>, 2.0 wt% GO/ $\alpha$ -AgVO<sub>3</sub>, and pure  $\alpha$ -AgVO<sub>3</sub> were successfully synthesized by a facile *in-situ* coprecipitation method, and their structure, morphology, photocatalytic performance, and mechanism were revealed. SEM analyses indicate that the as-prepared photocatalysts have a flower-like morphology, wherein the petals consist of  $\alpha$ -AgVO<sub>3</sub> nanorods with a length of a few microns and then GO nanosheets are uniformly covered on these nanorods. XRD analyses demonstrate that  $\alpha$ -AgVO<sub>3</sub> is well crystallized in a monoclinic  $\alpha$  phase with space group *C2/c*. Through the morphology and theoretical XRD pattern stimulation, it can be confirmed that the  $\alpha$ -AgVO<sub>3</sub> nanorods prefer to grow along the *c*-axis. Raman, FTIR, and XPS spectra analyses demonstrate the presence of GO nanosheets, and finally, confirm the formation of  $\alpha$ -AgVO<sub>3</sub> (002)//GO (002) heterojunction. The successful introduction of GO nanosheets and construction of heterostructure might have unique effect on the photocatalytic performance.

Compared with pure  $\alpha$ -AgVO<sub>3</sub> and other SVOs, 0.5 GO/ $\alpha$ -AgVO<sub>3</sub> displays the optimal photodegradation efficiency of 90% RhB removal with the maximum rate constant of 0.0584 min<sup>-1</sup> which is tens of times higher than that of pure  $\alpha$ -AgVO<sub>3</sub> and other SVOs.

Proper bandgap and efficient photocarrier separation play significant roles in high photocatalytic performance of GO/ $\alpha$ -AgVO<sub>3</sub>. Electronic structure and bandgap calculations by HSE03 functional and optical property analysis reveal that  $\alpha$ -AgVO<sub>3</sub> is a direct-gap semiconductor with a band gap of about 2.56 eV, which is suitable for visible-light absorption and irradiation. Then, the GO and  $\alpha$ -AgVO<sub>3</sub> heterojunction facilitates the transfer of photogenerated electrons, which overcomes the obstacle of rapid recombination of carriers and further boosts the photocatalytic activity. Moreover, some active species generated by the photochemical reaction can help degrade organic pollutants like RhB. With the advantage of suitable band gap, efficient photocarrier separation, and superior photocatalytic performance, GO/ $\alpha$ -AgVO<sub>3</sub> is a promising photocatalyst for the visible-light degradation of pollutants and water environmental protection.

### Acknowledgements

This work was financially supported by the National Natural Science Foundation of China (No. 52102068), the Key Laboratory Foundation of the Science and Technology on Advanced Functional Composite Laboratory (No. 6142906200509), the Natural Science Foundation of Jiangsu Province (No. 20KJB430017), NUPTSF (No. NY219162), and the Postgraduate Research & Practice Innovation Program of Jiangsu Province (No. KYCX20\_0789).

### Electronic Supplementary Material

Supplementary material is available in the online version of this article at <https://doi.org/10.1007/s40145-021-0534-6>.

### References

- [1] Hamdy MS, Abd-Rabboh HSM, Benaissa M, *et al.* Fabrication of novel polyaniline/ZnO heterojunction for exceptional photocatalytic hydrogen production and degradation of fluorescein dye through direct Z-scheme mechanism. *Opt Mater* 2021, **117**: 111198.
- [2] Al-Zaqri N, Alsalmeh A, Ahmed MA, *et al.* Construction of novel direct Z-scheme AgIO<sub>4</sub>-g-C<sub>3</sub>N<sub>4</sub> heterojunction for photocatalytic hydrogen production and photodegradation of fluorescein dye. *Diam Relat Mater* 2020, **109**: 108071.
- [3] Sadeghzadeh-Attar A. Photocatalytic degradation evaluation of N-Fe codoped aligned TiO<sub>2</sub> nanorods based on the effect of annealing temperature. *J Adv Ceram* 2020, **9**: 107–122.
- [4] Benaissa M, Abbas N, Al Arni S, *et al.* BiVO<sub>3</sub>/g-C<sub>3</sub>N<sub>4</sub> S-scheme heterojunction nanocomposite photocatalyst for hydrogen production and amaranth dye removal. *Opt Mater* 2021, **118**: 111237.
- [5] Zhou D, Chen YX, Yuan XY, *et al.* Self-induced synthesis under neutral conditions and novel visible light photocatalytic activity of Ag<sub>4</sub>V<sub>2</sub>O<sub>7</sub> polyoxometalate. *New J Chem* 2021, **45**: 9569–9581.
- [6] Su TM, Shao Q, Qin ZZ, *et al.* Role of interfaces in two-dimensional photocatalyst for water splitting. *ACS Catal* 2018, **8**: 2253–2276.
- [7] Chen MZ, Jia YM, Li HM, *et al.* Enhanced photocatalysis of the pyroelectric BiFeO<sub>3</sub>/g-C<sub>3</sub>N<sub>4</sub> heterostructure for dye decomposition driven by cold-hot temperature alternation. *J Adv Ceram* 2021, **10**: 338–346.
- [8] Zhao W, Guo Y, Wang SM, *et al.* A novel ternary plasmonic photocatalyst: Ultrathin g-C<sub>3</sub>N<sub>4</sub> nanosheet hybridized by Ag/AgVO<sub>3</sub> nanoribbons with enhanced visible-light photocatalytic performance. *Appl Catal B: Environ* 2015, **165**: 335–343.
- [9] Ahmed MA, Al-Zaqri N, Alsalmeh A, *et al.* Rapid photocatalytic degradation of RhB dye and photocatalytic hydrogen production on novel curcumin/SnO<sub>2</sub> nanocomposites through direct Z-scheme mechanism. *J Mater Sci: Mater Electron* 2020, **31**: 19188–19203.
- [10] Yuan XY, Wang FR, Liu JK, *et al.* Thermal perturbation nucleation and controllable growth of silver vanadate crystals by dynamic template route. *Cryst Growth Des* 2017, **17**: 4254–4264.
- [11] Chen YX, Liang Y, Zhao MJ, *et al.* *In situ* ion exchange synthesis of Ag<sub>2</sub>S/AgVO<sub>3</sub> graphene aerogels for enhancing photocatalytic antifouling efficiency. *Ind Eng Chem Res* 2019, **58**: 3538–3548.
- [12] Zhou D, Wang YY, Wang FR, *et al.* Design and application of Ag<sub>3</sub>PO<sub>4</sub>@Ag<sub>4</sub>V<sub>2</sub>O<sub>7</sub> Z-scheme photocatalysts with a micro-nano tube-cluster structure for the co-degradation of nitrate and ammonia in wastewater. *Ind Eng Chem Res* 2019, **58**: 18027–18035.
- [13] Ran R, Meng XC, Zhang ZS. Facile preparation of novel graphene oxide-modified Ag<sub>2</sub>O/Ag<sub>3</sub>VO<sub>4</sub>/AgVO<sub>3</sub> composites with high photocatalytic activities under visible light irradiation. *Appl Catal B: Environ* 2016, **196**: 1–15.
- [14] Shen GZ, Chen D. Self-coiling of Ag<sub>2</sub>V<sub>4</sub>O<sub>11</sub> nanobelts into perfect nanorings and microloops. *J Am Chem Soc* 2006, **128**: 11762–11763.
- [15] Zhao W, Guo Y, Faiz Y, *et al.* Facile *in-situ* synthesis of Ag/AgVO<sub>3</sub> one-dimensional hybrid nanoribbons with enhanced performance of plasmonic visible-light photocatalysis. *Appl Catal B: Environ* 2015, **163**: 288–297.
- [16] Yang YM, Liu YY, Huang BB, *et al.* Enhanced visible photocatalytic activity of a BiVO<sub>4</sub>@ $\beta$ -AgVO<sub>3</sub> composite synthesized by an *in situ* growth method. *RSC Adv* 2014, **4**: 20058–20061.
- [17] Sun M, Senthil RA, Pan JQ, *et al.* A facile synthesis of visible-light driven rod-on-rod like  $\alpha$ -FeOOH/ $\alpha$ -AgVO<sub>3</sub>

- nanocomposite as greatly enhanced photocatalyst for degradation of rhodamine B. *Catalysts* 2018, **8**: 392.
- [18] Chen LC, Teng CY, Lin CY, *et al.* Architecting nitrogen functionalities on graphene oxide photocatalysts for boosting hydrogen production in water decomposition process. *Adv Energy Mater* 2016, **6**: 1600719.
- [19] Huang YJ, Wan CL. Controllable fabrication and multifunctional applications of graphene/ceramic composites. *J Adv Ceram* 2020, **9**: 271–291.
- [20] Tian HW, Liu M, Zheng WT. Constructing 2D graphitic carbon nitride nanosheets/layered MoS<sub>2</sub>/graphene ternary nanojunction with enhanced photocatalytic activity. *Appl Catal B: Environ* 2018, **225**: 468–476.
- [21] Clark SJ, Segall MD, Pickard CJ, *et al.* First principles methods using CASTEP. *Zeitschrift Für Kristallographie Cryst Mater* 2005, **220**: 567–570.
- [22] Segall MD, Lindan PJD, Probert MJ, *et al.* First-principles simulation: Ideas, illustrations and the CASTEP code. *J Phys: Condens Matter* 2002, **14**: 2717–2744.
- [23] Pack JD, Monkhorst HJ. “Special points for Brillouin-zone integrations”—A reply. *Phys Rev B* 1977, **16**: 1748–1749.
- [24] Perdew JP, Burke K, Ernzerhof M. Generalized gradient approximation made simple. *Phys Rev Lett* 1996, **77**: 3865–3868.
- [25] Zhou YC, Xiang HM. Al<sub>3</sub>BO<sub>9</sub>: A wide band gap, damage-tolerant, and thermal insulating lightweight material for high-temperature applications. *J Am Ceram Soc* 2016, **99**: 2742–2751.
- [26] Donnay JDH, Harker D. A new law of crystal morphology extending the Law of Bravais. *Am Mineral* 1937, **22**: 446–467.
- [27] Wells AF. XXI. crystal habit and internal structure.—I. *The London, Edinburgh, and Dublin Philosophical Magazine and Journal of Science* 1946, **37**: 184–199.
- [28] Berkovitch-Yellin Z. Toward an *ab initio* derivation of crystal morphology. *J Am Chem Soc* 1985, **107**: 8239–8253.
- [29] Sivakumar V, Suresh R, Giribabu K, *et al.* AgVO<sub>3</sub> nanorods: Synthesis, characterization and visible light photocatalytic activity. *Solid State Sci* 2015, **39**: 34–39.
- [30] Barebita H, Ferraa S, Moutataouia M, *et al.* Structural investigation of Bi<sub>2</sub>O<sub>3</sub>–P<sub>2</sub>O<sub>5</sub>–B<sub>2</sub>O<sub>3</sub>–V<sub>2</sub>O<sub>5</sub> quaternary glass system by Raman, FTIR and thermal analysis. *Chem Phys Lett* 2020, **760**: 138031.
- [31] Li Q, Guo B, Yu J, *et al.* Highly efficient visible-light-driven photocatalytic hydrogen production of CdS-cluster-decorated graphene nanosheets. *J Am Chem Soc* 2011, **133**: 10878–10884.
- [32] Wang H, Robinson JT, Li X, *et al.* Solvothermal reduction of chemically exfoliated graphene sheets. *J Am Chem Soc* 2009, **131**: 9910–9911.
- [33] Zhao W, Li JH, Wei ZB, *et al.* Fabrication of a ternary plasmonic photocatalyst of Ag/AgVO<sub>3</sub>/RGO and its excellent visible-light photocatalytic activity. *Appl Catal B: Environ* 2015, **179**: 9–20.
- [34] Kong XG, Guo ZL, Zeng CB, *et al.* Soft chemical *in situ* synthesis, formation mechanism and electrochemical performances of 1D bead-like AgVO<sub>3</sub> nanoarchitectures. *J Mater Chem A* 2015, **3**: 18127–18135.
- [35] de Oliveira RC, de Foggi CC, Teixeira MM, *et al.* Mechanism of antibacterial activity via morphology change of  $\alpha$ -AgVO<sub>3</sub>: Theoretical and experimental insights. *ACS Appl Mater Interfaces* 2017, **9**: 11472–11481.
- [36] Singh DP, Polychronopoulou K, Rebholz C, *et al.* Room temperature synthesis and high temperature frictional study of silver vanadate nanorods. *Nanotechnology* 2010, **21**: 325601.
- [37] Wang F, Li F, Zhang LF, *et al.* S–TiO<sub>2</sub> with enhanced visible-light photocatalytic activity derived from TiS<sub>2</sub> in deionized water. *Mater Res Bull* 2017, **87**: 20–26.
- [38] Gao L, Li ZH, Liu JW. Facile synthesis of Ag<sub>3</sub>VO<sub>4</sub>/ $\beta$ -AgVO<sub>3</sub> nanowires with efficient visible-light photocatalytic activity. *RSC Adv* 2017, **7**: 27515–27521.
- [39] Wang R, Cao L. Facile synthesis of a novel visible-light-driven AgVO<sub>3</sub>/BiVO<sub>4</sub> heterojunction photocatalyst and mechanism insight. *J Alloys Compd* 2017, **722**: 445–451.
- [40] Zhang J, Wang J, Xu HH, *et al.* The effective photocatalysis and antibacterial properties of AgBr/AgVO<sub>3</sub> composites under visible-light. *RSC Adv* 2019, **9**: 37109–37118.
- [41] Wang JX, Yang X, Chen J, *et al.* Photocatalytic activity of novel Ag<sub>4</sub>V<sub>2</sub>O<sub>7</sub> photocatalyst under visible light irradiation. *J Am Ceram Soc* 2014, **97**: 267–274.
- [42] Zhang TT, Zhao DF, Wang Y, *et al.* Facial synthesis of a novel Ag<sub>4</sub>V<sub>2</sub>O<sub>7</sub>/g-C<sub>3</sub>N<sub>4</sub> heterostructure with highly efficient photoactivity. *J Am Ceram Soc* 2019, **102**: 3897–3907.
- [43] Zhang L, He YM, Ye P, *et al.* Enhanced photodegradation activity of rhodamine B by Co<sub>3</sub>O<sub>4</sub>/Ag<sub>3</sub>VO<sub>4</sub> under visible light irradiation. *Mater Sci Eng: B* 2013, **178**: 45–52.
- [44] Perdew JP, Ruzsinszky A, Csonka GI, *et al.* Restoring the density-gradient expansion for exchange in solids and surfaces. *Phys Rev Lett* 2008, **100**: 136406.
- [45] Heyd J, Scuseria GE, Ernzerhof M. Hybrid functionals based on a screened Coulomb potential. *J Chem Phys* 2003, **118**: 8207–8215.
- [46] Tandon SP, Gupta JP. Measurement of forbidden energy gap of semiconductors by diffuse reflectance technique. *Phys Status Solidi B* 1970, **38**: 363–367.
- [47] Liu J, Liu Y, Liu N, *et al.* Metal-free efficient photocatalyst for stable visible water splitting via a two-electron pathway. *Science* 2015, **347**: 970–974.
- [48] Wu XQ, Zhao J, Wang LP, *et al.* Carbon dots as solid-state electron mediator for BiVO<sub>4</sub>/CDs/CdS Z-scheme photocatalyst working under visible light. *Appl Catal B: Environ* 2017, **206**: 501–509.
- [49] Zheng Y, Yu ZH, Ou HH, *et al.* Black phosphorus and polymeric carbon nitride heterostructure for photoinduced molecular oxygen activation. *Adv Funct Mater* 2018, **28**: 1705407.
- [50] Luo G, Jiang X, Li M, *et al.* Facile fabrication and enhanced photocatalytic performance of Ag/AgCl/rGO heterostructure photocatalyst. *ACS Appl Mater Interfaces* 2013, **5**: 2161–2168.
- [51] Liu DN, Chen DY, Li NJ, *et al.* Integration of 3D

- macroscopic graphene aerogel with 0D-2D AgVO<sub>3</sub>-g-C<sub>3</sub>N<sub>4</sub> heterojunction for highly efficient photocatalytic oxidation of nitric oxide. *Appl Catal B: Environ* 2019, **243**: 576–584.
- [52] Ran R, McEvoy JG, Zhang ZS. Ag<sub>2</sub>O/Ag<sub>3</sub>VO<sub>4</sub>/Ag<sub>4</sub>V<sub>2</sub>O<sub>7</sub> heterogeneous photocatalyst prepared by a facile hydrothermal synthesis with enhanced photocatalytic performance under visible light irradiation. *Mater Res Bull* 2016, **74**: 140–150.
- [53] Yang WY, Chen Y, Gao S, *et al.* Post-illumination activity of Bi<sub>2</sub>WO<sub>6</sub> in the dark from the photocatalytic “memory” effect. *J Adv Ceram* 2021, **10**: 355–367.
- [54] Cao SY, Liu TG, Tsang Y, *et al.* Role of hydroxylation modification on the structure and property of reduced graphene oxide/TiO<sub>2</sub> hybrids. *Appl Surf Sci* 2016, **382**: 225–238.

**Open Access** This article is licensed under a Creative Commons Attribution 4.0 International License, which permits use, sharing, adaptation, distribution and reproduction in any medium or format, as long as you give appropriate credit to the original author(s) and the source, provide a link to the Creative Commons licence, and indicate if changes were made.

The images or other third party material in this article are included in the article’s Creative Commons licence, unless indicated otherwise in a credit line to the material. If material is not included in the article’s Creative Commons licence and your intended use is not permitted by statutory regulation or exceeds the permitted use, you will need to obtain permission directly from the copyright holder.

To view a copy of this licence, visit <http://creativecommons.org/licenses/by/4.0/>.